nature physics

SUPPLEMENTARY INFORMATION

https://doi.org/10.1038/s41567-020-0836-6

In the format provided by the authors and unedited.

Non-Hermitian bulk–boundary correspondence in quantum dynamics

Lei Xiao[1,5], Tianshu Deng[2,5], Kunkun Wang[1], Gaoyan Zhu[1], Zhong Wang[3]✉, Wei Yi[2,4]✉ and Peng Xue[1]✉

[1]Beijing Computational Science Research Center, Beijing, China. [2]CAS Key Laboratory of Quantum Information, University of Science and Technology of China, Hefei, China. [3]Institute for Advanced Study, Tsinghua University, Beijing, China. [4]CAS Center for Excellence in Quantum Information and Quantum Physics, Hefei, China. [5]These authors contributed equally: Lei Xiao, Tianshu Deng. ✉e-mail: wangzhongemail@tsinghua.edu.cn; wyiz@ustc.edu.cn; gnep.eux@gmail.com

SUPPLEMENTAL INFORMATION FOR "NON-HERMITIAN BULK-BOUNDARY CORRESPONDENCE IN QUANTUM DYNAMICS"

In this Supplemental Information, we provide the details on calculations of the effective Hamiltonian, generalized Brillouin zone, non-Bloch topological invariants, and additional supporting experimental data.

Effective Hamiltonian of discrete-time quantum-walk dynamics

In this section, we derive a formal expression for the effective Hamiltonian $H_{\text{eff}}(k)$ in momentum space. We start from the Fourier component of U

$$U(k) = d_0\sigma_0 - id_1\sigma_x - id_2\sigma_y - id_3\sigma_z, \tag{S1}$$

where

$$\begin{aligned} d_0 &= -\cosh\gamma\sin\theta_1\sin\theta_2 + \cosh\gamma\cos k\cos\theta_1\cos\theta_2 + i\sinh\gamma\cos\theta_1\sin k, \\ d_1 &= 0, \\ d_2 &= \cosh\gamma\cos\theta_1\sin\theta_2 + \cos k\cosh\gamma\cos\theta_2\sin\theta_1 + i\sin k\sinh\gamma\sin\theta_1, \\ d_3 &= -\sin k\cosh\gamma\cos\theta_2 + i\cos k\sinh\gamma. \end{aligned} \tag{S2}$$

Here $\sigma_{x,y,z}$ are the standard Pauli matrices and σ_0 is the 2-by-2 identity matrix. Near $k = 0$, d_3 resembles the $\sin k + i\gamma/2$ term appearing in the non-Hermitian Su-Schrieffer-Heeger model with non-Hermitian skin effect [1], which provides an intuitive understanding for the skin effect of U.

Since the effective Hamiltonian $H_{\text{eff}}(k)$ is related to $U(k)$ through $U = e^{-iH_{\text{eff}}}$, the right- and left-eigenvectors of $H_{\text{eff}}(k)$ can be defined through $U(k)$, with $U(k)|\psi_\pm\rangle = \lambda_\pm|\psi_\pm\rangle$ and $[U^{-1}(k)]^\dagger|\chi_\pm\rangle = (\lambda_\pm^*)^{-1}|\chi_\pm\rangle$. Here $\lambda_\pm = d_0 \pm D_k$, and $D_k := i\sqrt{d_1^2 + d_2^2 + d_3^2}$. It is straightforward to derive

$$|\psi_\pm\rangle = \frac{1}{\sqrt{-2D_k^2 \mp 2id_3D_k}} \begin{pmatrix} -id_1 - d_2 \\ \pm D_k + id_3 \end{pmatrix}, \tag{S3}$$

$$|\chi_\pm\rangle = \frac{1}{\sqrt{-2D_k^2 \mp 2id_3D_k}} \begin{pmatrix} -id_1^* - d_2^* \\ \mp D_k^* + id_3^* \end{pmatrix}. \tag{S4}$$

It follows that

$$U(k) = \lambda_+\frac{|\psi_+\rangle\langle\chi_+|}{\langle\chi_+|\psi_+\rangle} + \lambda_-\frac{|\psi_-\rangle\langle\chi_-|}{\langle\chi_-|\psi_-\rangle}, \tag{S5}$$

from which a formal expression of $H_{\text{eff}}(k)$ can be written as

$$H_{\text{eff}}(k) = i\Big[\ln(\lambda_+)\frac{|\psi_+\rangle\langle\chi_+|}{\langle\chi_+|\psi_+\rangle} + \ln(\lambda_-)\frac{|\psi_-\rangle\langle\chi_-|}{\langle\chi_-|\psi_-\rangle}\Big]. \tag{S6}$$

Note that Eq. (S6) is already quite complicated, which is even more so when transformed back into the coordinate space. Therefore, it is cubersome to directly characterize H_{eff}, and we opt to focus on the Floquet operator U, which is indeed the common practice in the study of discrete-time quantum-walk dynamics. Despite the lack of a simple form, H_{eff} is a non-Hermitian, chiral symmetric Hamiltonian, which features non-Hermitian skin effects and the breakdown of conventional bulk-boundary correspondence.

Non-Bloch band theory: Bulk-state wave functions, generalized Brillouin zones, and non-Bloch topological invariants

In this section, we outline the calculation of generalized Brillouin zones and non-Bloch topological invariants in our quantum-walk system. We closely follow the non-Bloch band theory in Refs. [1] and [2], where similar quantities for a static non-Hermitian SSH model are derived. Whereas characterizing quantum-walk dynamics is more complicated due to an enlarged parameter space, the general recipe remains the same: (i) write down the ansatz wave function

of the bulk states, whose variational parameters (the spatial-mode functions $\beta_{\alpha,j}$ in the main text) underlie the non-Hermitian skin effect; (ii) derive a set of linear equations from the eigen-equation of U (or the Schr odinger's equation in the static case), both in the bulk and at boundaries; (iii) send the coefficient matrix of the linear equations to zero in the thermodynamic limit, which allows for the solution of the eigenspectrum of U, as well as spatial-mode functions; (iv) determine the generalized Billouin zones and non-Bloch topological invariants.

For the convenience of derivation, let us first re-write the Floquet operator in the main text as $U = FMG$, with

$$\begin{aligned} F &= R[\frac{\theta_1(x)}{2}]S_2R[\frac{\theta_2(x)}{2}], \\ G &= R[\frac{\theta_2(x)}{2}]S_1R[\frac{\theta_1(x)}{2}], \end{aligned} \tag{S7}$$

where the coin-rotation operator R and the shift operator S are given by

$$\begin{aligned} R(\theta) &= \mathbb{1}_w \otimes e^{-i\theta\sigma_y}, \\ S_1 &= \sum_x |x\rangle\langle x| \otimes |0\rangle\langle 0| + |x+1\rangle\langle x| \otimes |1\rangle\langle 1|, \\ S_2 &= \sum_x |x-1\rangle\langle x| \otimes |0\rangle\langle 0| + |x\rangle\langle x| \otimes |1\rangle\langle 1|. \end{aligned} \tag{S8}$$

Here $\sigma_y = i(|1\rangle\langle 0| - |0\rangle\langle 1|)$ is the y Pauli matrix, $\mathbb{1}_w = \sum_x |x\rangle\langle x|$, and $-N \leqslant x \leqslant N-1$ is the site index of the lattice. For a domain-wall configuration on a circle with $2N$ lattice sites (see Fig. 1 of the main text), we adopt a cyclic index such that $|x-1\rangle|_{x=-N} = |N-1\rangle$ and $|x+1\rangle|_{x=N-1} = |-N\rangle$. We also have

$$\begin{cases} \theta_{1(2)}(x) = \theta^L_{1(2)} & x \in J_L \\ \theta_{1(2)}(x) = \theta^R_{1(2)} & x \in J_R \end{cases}, \tag{S9}$$

where $\theta^\alpha_{1(2)}$ represent coin parameters of the left ($\alpha = L$) and right ($\alpha = R$) bulk, $J_L = \{x \in \mathbb{Z} | -N \leqslant x \leqslant -1\}$ and $J_R = \{x \in \mathbb{Z} | 0 \leqslant x \leqslant N-1\}$.

We then rewrite U as

$$U = \sum_x \Big[|x\rangle\langle x+1| \otimes A_m(x) + |x\rangle\langle x-1| \otimes A_p(x) + |x\rangle\langle x| \otimes A_s(x)\Big], \tag{S10}$$

where the site-dependent coin-state operators $A_{m,p,s}(x)$ are given by

$$\begin{aligned} A_m(x) &= F_m(x+1)MG_s(x+1), \\ A_p(x) &= F_s(x)MG_p(x-1), \\ A_s(x) &= F_s(x)MG_s(x) + F_m(x+1)MG_p(x), \end{aligned} \tag{S11}$$

with

$$\begin{aligned} F_m(x) &= R[\frac{\theta_1(x-1)}{2}]P_0R[\frac{\theta_2(x)}{2}], \\ F_s(x) &= R[\frac{\theta_1(x)}{2}]P_1R[\frac{\theta_2(x)}{2}], \\ G_s(x) &= R[\frac{\theta_2(x)}{2}]P_0R[\frac{\theta_1(x)}{2}], \\ G_p(x) &= R[\frac{\theta_2(x+1)}{2}]P_1R[\frac{\theta_1(x)}{2}], \end{aligned} \tag{S12}$$

and $P_0 = |0\rangle\langle 0|$, $P_1 = |1\rangle\langle 1|$.

After these preparatory works, we write down the general eigenstate of U as $|\psi\rangle = |\psi^R\rangle + |\psi^L\rangle$, with [1, 2]

$$|\psi^\alpha\rangle = \sum_{x\in J_\alpha, j} \beta^x_{\alpha,j}|x\rangle \otimes |\phi^\alpha_j\rangle_c \quad (\alpha = L, R), \tag{S13}$$

where $|\phi^\alpha\rangle_c$ is the coin state of the corresponding bulk and β_α is the spatial-mode function.

Substituting the eigenstate wave function into the eigen-equation $U|\psi\rangle = \lambda|\psi\rangle$, we have

$$\left(A_m^\alpha \beta_\alpha + \frac{A_p^\alpha}{\beta_\alpha} + A_s^\alpha - \lambda\right)|\phi^\alpha\rangle_c = 0, \tag{S14}$$

where $A_{m,p,s}^\alpha$ are the corresponding coin operators in the bulk, with $A_{m,p,s}^L = A_{m,p,s}(x)$ $(-N+1 \leqslant x \leqslant -2)$ and $A_{m,p,s}^R = A_{m,p,s}(x)$ $(1 \leqslant x \leqslant N-2)$.

Equation (S14) supports non-trivial solutions when

$$\det\left[A_m^\alpha \beta_\alpha + A_p^\alpha \frac{1}{\beta_\alpha} + A_s^\alpha - \lambda\right] = 0. \tag{S15}$$

Eq. (S15) appears to be a quartic equation of β_α, however, it is in fact quadratic because, as a consequence of $\det A_m^\alpha = \det A_p^\alpha = 0$, the coefficients of β_α^2 and β_α^{-2} vanish. As such, it has two solutions denoted by $\beta_{\alpha,j}$ with $j = 1, 2$. Correspondingly, eigenstates of the bulk can be written as

$$|\psi^\alpha\rangle = \sum_{x\in J_\alpha, j=1,2} \beta_{\alpha,j}^x |x\rangle \otimes |\phi_j^\alpha\rangle_c. \tag{S16}$$

The domain-wall boundary condition is enforced by substituting Eq. (S16) into $U|\psi\rangle = \lambda|\psi\rangle$ at the boundaries $(x = -N, -1, 0, N-1)$. Making use of Eq. (S14), we derive a set of linear equations $M\left[|\phi_1^L\rangle_c, |\phi_2^L\rangle_c, |\phi_1^R\rangle_c, |\phi_2^R\rangle_c\right]^T = 0$, where

$$M = \begin{pmatrix} -A_p^L \beta_{L,1}^{-N-1} & -A_p^L \beta_{L,2}^{-N-1} & A_p(-N)\beta_{R,1}^{N-1} & A_p(-N)\beta_{R,2}^{N-1} \\ A_p^L \beta_{L,1}^{-2} + [A_s(-1) - \beta]\beta_{L,1}^{-1} & A_p^L \beta_{L,2}^{-2} + [A_s(-1) - \lambda]\beta_{L,2}^{-1} & A_m(-1) & A_m(-1) \\ A_p(0)\beta_{L,1}^{-1} & A_p(0)\beta_{L,2}^{-1} & -A_p^R \beta_{R,1}^{-1} & -A_p^R \beta_{R,2}^{-1} \\ A_m(N-1)\beta_{L,1}^{-N} & A_m(N-1)\beta_{L,2}^{-N} & A_p^R \beta_{R,1}^{N-2} + [A_s(N-1) - \lambda]\beta_{R,1}^{N-1} & A_p^R \beta_{R,2}^{N-2} + [A_s(N-1) - \lambda]\beta_{R,2}^{N-1} \end{pmatrix} \tag{S17}$$

Non-trivial solutions exist only when the 8-by-8 coefficient matrix M satisfies $\det(M) = 0$ in the thermodynamic limit $N \to \infty$. Because the $\sigma_z = -1$ components in $\left[|\phi_1^L\rangle_c, |\phi_2^L\rangle_c, |\phi_1^R\rangle_c, |\phi_2^R\rangle_c\right]^T$ are related to the $\sigma_z = +1$ components by Eq. (S14), the linear equations $M\left[|\phi_1^L\rangle_c, |\phi_2^L\rangle_c, |\phi_1^R\rangle_c, |\phi_2^R\rangle_c\right]^T = 0$ can be decomposed to equations for the four $\sigma_z = +1$ components. Requiring that the determinant of the 4-by-4 coefficient matrix vanishes, we have

$$a_1 \frac{1}{\beta_{L,1}^N}\beta_{R,1}^N + a_2 \frac{1}{\beta_{L,2}^N}\beta_{R,1}^N + a_3 \frac{1}{\beta_{L,1}^N}\beta_{R,2}^N + a_4 \frac{1}{\beta_{L,2}^N}\beta_{R,2}^N + b_L \frac{1}{\beta_{L,1}^N}\frac{1}{\beta_{L,2}^N} + b_R \beta_{R,1}^N \beta_{R,2}^N = 0, \tag{S18}$$

where $\{a_1, a_2, a_3, a_4, b_L, b_R\}$ are some coefficients whose exact forms are not important for the following discussion. Similar equations have appeared in the calculation of the generalized Brillouin zone for the non-Hermitian SSH model[1, 2].

To proceed further, we need to sort the following terms

$$\left\{|\frac{\beta_{R,1}}{\beta_{L,1}}|, |\frac{\beta_{R,1}}{\beta_{L,2}}|, |\frac{\beta_{R,2}}{\beta_{L,1}}|, |\frac{\beta_{R,2}}{\beta_{L,2}}|, |\frac{1}{\beta_{L,1}\beta_{L,2}}|, |\beta_{R,1}\beta_{R,2}|\right\}. \tag{S19}$$

This is because in the thermodynamic limit $(N \to \infty)$, only terms with the largest absolute values survive in Eq. (S18). Without loss of generality, we take $|\beta_{\alpha,1}| \geqslant |\beta_{\alpha,2}|$ and discuss the order of these terms case by case. For example, when $|\beta_{L,2}\beta_{R,2}| \leqslant 1$, $|\beta_{L,2}\beta_{R,1}| \leqslant 1$, and $|\beta_{L,1}\beta_{R,2}| \leqslant 1$, the largest two terms are $|\frac{1}{\beta_{L,1}\beta_{L,2}}|$ and $|\frac{\beta_{R,1}}{\beta_{L,2}}|$. Eq. (S18) is then reduced to

$$a_2 \frac{1}{\beta_{L,2}^N}\beta_{R,1}^N + b_L \frac{1}{\beta_{L,1}^N}\frac{1}{\beta_{L,2}^N} = 0. \tag{S20}$$

It follows that, in the thermodynamic limit, $|\beta_{L,1}\beta_{R,1}| = 1$.

Exhausting all the possible scenarios, we rewrite Eq. (S18) as

$$\zeta(\beta_{\alpha,j}) = 0, \tag{S21}$$

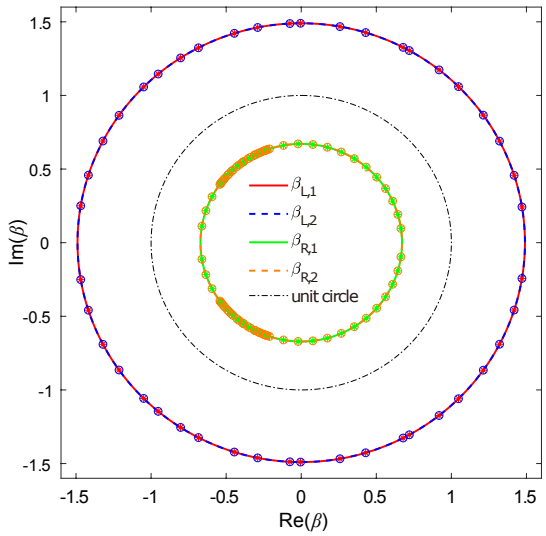

FIG. S1. **Numerical check of the ζ-function formula of generalized Brillouin zone.** Generalized Brillouin zones calculated from Eq. (S21) (solid and dashed lines), compared to those obtained from the numerically calculated eigenenergy spectrum (circles and asterisks). In the latter approach, we numerically calculate the λ eigenspectrum by diagonalizing U of a finite size system, and then obtain $\beta_{\alpha,j}$ from Eq. (S15). The two approaches lead to consistent results, confirming the validity of Eq. (S21) as the equation of generalized Brillouin zone. In this figure, we take the same parameters as those in Fig. 4b of the main text.

where

$$\zeta(\beta_{\alpha,j}) := \begin{cases} |\beta_{L,1}\beta_{R,1}| - 1, & |\beta_{L,2}\beta_{R,2}| \leqslant 1 \text{ and } |\beta_{L,2}\beta_{R,1}| \leqslant 1 \text{ and } |\beta_{L,1}\beta_{R,2}| \leqslant 1, \\ |\beta_{L,2}\beta_{R,2}| - 1, & |\beta_{L,1}\beta_{R,1}| \geqslant 1 \text{ and } |\beta_{L,1}\beta_{R,2}| \geqslant 1 \text{ and } |\beta_{L,2}\beta_{R,1}| \geqslant 1, \\ |\beta_{L,1}| - |\beta_{L,2}|, & |\beta_{L,2}\beta_{R,1}| \geqslant 1 \text{ and } |\beta_{L,1}\beta_{R,2}| \leqslant 1, \\ |\beta_{R,1}| - |\beta_{R,2}|, & |\beta_{L,1}\beta_{R,2}| \geqslant 1 \text{ and } |\beta_{L,2}\beta_{R,1}| \leqslant 1. \end{cases} \tag{S22}$$

Note that $\zeta(\beta_{\alpha,j})$ is a function of λ since $\beta_{\alpha,j}$ are functions of λ through Eq. (S15). Therefore, we can solve Eq. (S21) as an equation of λ, and find the λ eigenspectrum. From the λ eigenspectrum we can obtain $\beta_{\alpha,j}$ by Eq. (S15). The $\beta_{\alpha,j}$ trajectories are the generalized Brillouin zones, which play a key role in the non-Hermitian bulk-boundary correspondence. The obtained generalized Brillouin zones are shown in Fig. S1. To double check the validity of Eq. (S21) as the equation of generalized Brillouin zone, we also numerically diagonalize U for finite-size systems, and then obtain the corresponding $\beta_{\alpha,j}$ by Eq. (S15). The generalized Brillouin zones obtained in this way are consistent with those obtained from Eq. (S21) [see Fig. S1].

Finally, we note that Eq. (S22) is helpful in identifying generalized Brillouin zones of the two bulks from numerically calculated eigenspectrum. Specifically, eigenstates of U belonging to the first and second cases are associated with the generalized Brillouin zones of both bulks; whereas those belonging to the third (fourth) case are associated only with the generalized Brillouin zone of the left (right) bulk. In fact, the equations for the third and fourth cases in Eq. (S22) are the same as those of a single bulk without domain wall, as obtained in Ref. [1].

Based on the generalized Brillouin zones, we then calculate the non-Bloch topological invariants $\tilde{\nu}_\epsilon$ ($\epsilon = 0, \pi$) defined in the main text. The results precisely match the topological edge modes with $\epsilon = 0, \pi$ respectively, which embodies the non-Hermitian bulk-boundary correspondence.

An alternative approach to calculate non-Bloch topological invariants: Non-Bloch winding numbers in different time frames

In this section, we provide an alternative approach to calculate the non-Bloch topological invariants. The idea is to calculate the non-Bloch winding numbers in different time frames of the Floquet sequence. In the Hermitian case, this approach has been adopted in Ref. [3] to calculate the Bloch topological invariants. The obtained topological invariants $\tilde{\nu}_0$ and $\tilde{\nu}_\pi$ below are the same as those calculated from the periodized Floquet operators $\overline{U}_\epsilon$.

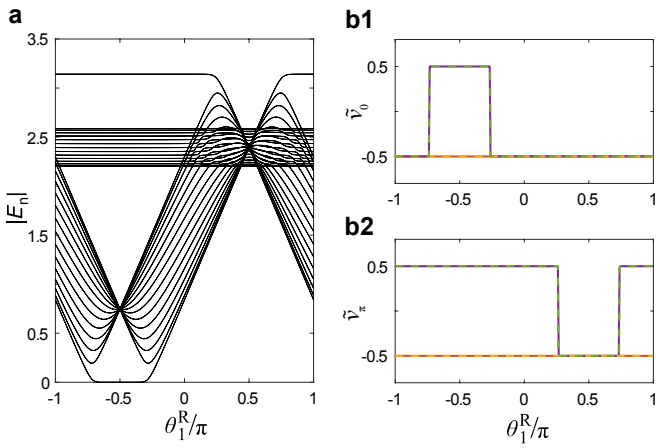

FIG. S2. **Calculation of the non-Bloch topological invariants.** **a** The absolute values of the quasienergy spectrum as a function of θ_1^R. The parameters are the same as those in Fig. 4a of the main text, where the quasienergy spectrum is completely real. **b1, b2** Non-Bloch topological invariants of the left (red solid line) and right bulks (purple solid line) using periodized Floquet operators, as outlined in the main text. We also show non-Bloch topological invariants calculated using the two different time frames, for the left (yellow dashed line) and right bulks (green dashed line).

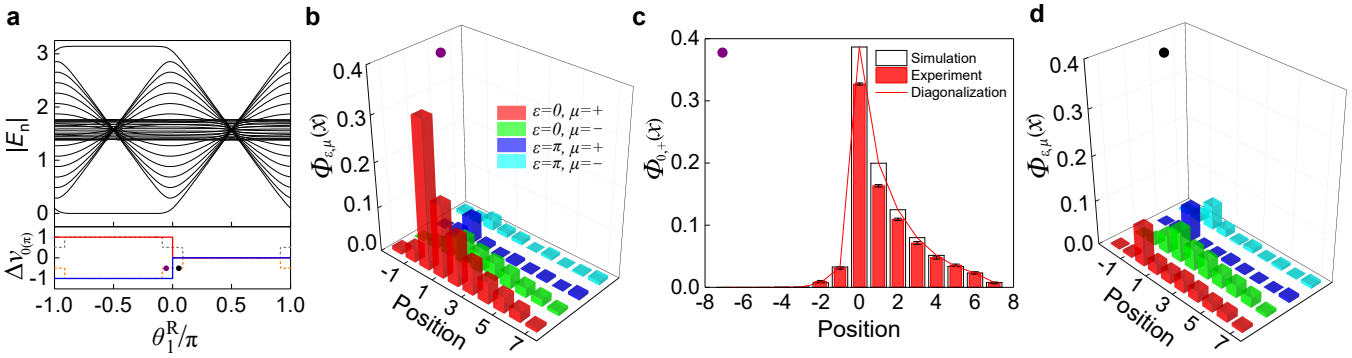

FIG. S3. **Non-Bloch bulk-boundary correspondence in the alternative time frame given by U'.** **a** Quasi-energy spectrum (black), and winding-number differences for the zero- (red) and π-modes (blue) between the two bulks with the parameters: $\theta_1^L = 0.5625\pi$, $\theta_2^R = 0$, $\theta_2^L = \pi$, and $\gamma = 0.2746$. The purple dot with $\theta_1^R = -0.0667\pi$ corresponds to the parameter used in **b**, where the system possesses both zero- and π-mode edge states. The black dot with $\theta_1^R = 0.0667\pi$ corresponds to the parameter used in **d**, where there is no edge state. **b** Experimentally measured $\Phi_{\epsilon,\mu}(x)$ after the seventh step with the initial state $|0\rangle\otimes|+\rangle$. **c** Comparison between experimentally-measured and numerically-calculated $\Phi_{0,+}(x)$, as well as the scaled norms of the corresponding edge state after the seventh step. Topological edge states are numerically calculated for a domain-wall system with $N = 15$, whose norms are scaled to fit the central peak of the corresponding $\Phi_{0,+}(x)$. **d** Experimentally measured $\Phi_{\epsilon,\mu}(x)$ after the seventh step with the same initial state as **b**. Error bars represent standard deviations due to photon-counting statistics.

First, we demonstrate how to calculate winding numbers in the time frame defined by U. From Eq. (S1), the Fourier component of U in the two bulks can be written as

$$U^\alpha(k) = d_0^\alpha \sigma_0 - i d_1^\alpha \sigma_x - i d_2^\alpha \sigma_y - i d_3^\alpha \sigma_z, \tag{S23}$$

where

$$\begin{aligned}
d_0^\alpha &= -\cosh\gamma \sin\theta_1^\alpha \sin\theta_2^\alpha + \cosh\gamma \cos k \cos\theta_1^\alpha \cos\theta_2^\alpha + i \sinh\gamma \cos\theta_1^\alpha \sin k, \\
d_1^\alpha &= 0, \\
d_2^\alpha &= \cosh\gamma \cos\theta_1^\alpha \sin\theta_2^\alpha + \cos k \cosh\gamma \cos\theta_2^\alpha \sin\theta_1^\alpha + i \sin k \sinh\gamma \sin\theta_1^\alpha, \\
d_3^\alpha &= -\sin k \cosh\gamma \cos\theta_2^\alpha + i \cos k \sinh\gamma.
\end{aligned} \tag{S24}$$

To calculate the Bloch winding numbers, we follow the standard practice and apply a unitary transformation

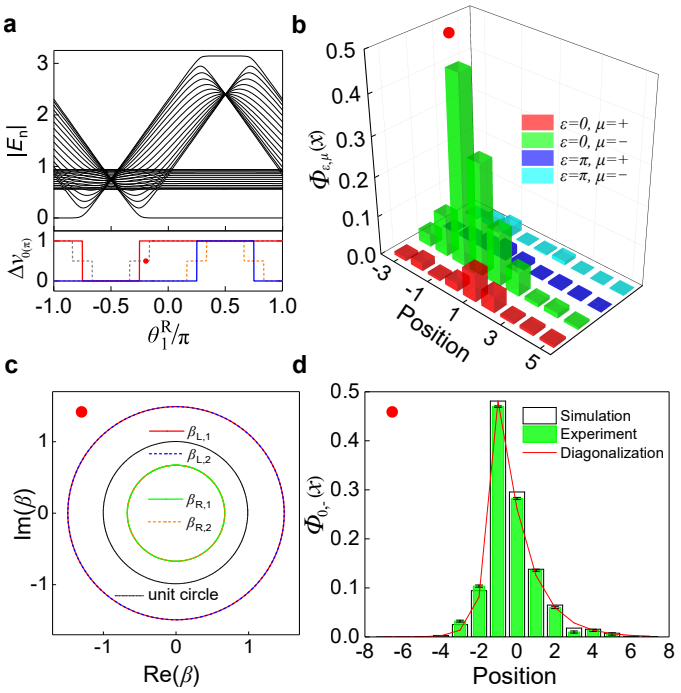

FIG. S4. **Non-Bloch bulk-boundary correspondence for edge states with $\epsilon = 0$. a** Quasi-energy spectrum (black), and winding-number differences $\Delta\tilde{\nu}_0$ (red) and $\Delta\tilde{\nu}_\pi$ (blue) between the two bulks with the parameters: $\theta_1^L = -0.5625\pi$, $\theta_2^R = 0.25\pi$, $\theta_2^L = 0.75\pi$, and $\gamma = 0.2746$. Color and line shapes for winding numbers are the same as in Fig. 4 of the main text. The red dot with $\theta_1^R = -0.18\pi$ corresponds to the coin parameter used in **b, d**, where only one topological edge state exists, consistent with measurement in **b**. **b** Experimentally measured $\Phi_{\epsilon,\mu}(x)$ after the seventh step with the initial state $|0\rangle \otimes |-\rangle$. **c** Generalized Brillouin zones on the complex plane. **d** Comparison between experimentally-measured and numerically-calculated $\Phi_{0,-}(x)$, as well as the scaled norms of the topological edge state after the seventh step. Error bars represent standard deviations due to photon-counting statistics.

$V = \exp(i\frac{\pi}{4}\sigma_y)$ to $U^\alpha(k)$ such that

$$W^\alpha(k) = VU^\alpha(k)V^\dagger = d_0^\alpha I - i(-d_3^\alpha)\sigma_x - id_2^\alpha\sigma_y - id_1^\alpha\sigma_z. \tag{S25}$$

The Bloch winding number is then defined through the generalized Zak phase

$$\nu^\alpha = \frac{\phi_{\text{Zak}}^\alpha}{\pi}, \tag{S26}$$

$$\phi_{\text{Zak}}^\alpha = \int_{-\pi}^{\pi} dk \frac{\langle\chi_k^\alpha|i\partial_k|\psi_k^\alpha\rangle}{\langle\chi_k^\alpha|\psi_k^\alpha\rangle}, \tag{S27}$$

where $|\psi_k^\alpha\rangle$ and $|\chi_k^\alpha\rangle$ are the right and left eigenstates of $W^\alpha(k)$ with

$$W^\alpha|\psi_k^\alpha\rangle = \lambda_k^\alpha|\psi_k^\alpha\rangle, \tag{S28}$$

$$[(W^\alpha)^{-1}]^\dagger|\chi_k^\alpha\rangle = \lambda_k^{\alpha*}|\chi_k^\alpha\rangle, \tag{S29}$$

$$\lambda_k^\alpha = d_0^\alpha - i\sqrt{(d_1^\alpha)^2 + (d_2^\alpha)^2 + (d_3^\alpha)^2}. \tag{S30}$$

From the above equations, we have

$$\nu^\alpha = \frac{1}{2\pi}\int dk \frac{-d_3^\alpha\frac{\partial d_2^\alpha}{\partial k} + d_2^\alpha\frac{\partial d_3^\alpha}{\partial k}}{(d_3^\alpha)^2 + (d_2^\alpha)^2}. \tag{S31}$$

In contrast, under the non-Hermitian skin effect, bulk states become localized, therefore we need the non-Bloch winding numbers calculated along the generalized Brillouin zones. From the spatial-mode function $\beta_{\alpha,j}$, we define

$$\beta_{\alpha,j} = |\beta_{\alpha,j}(p_j^\alpha)|e^{ip_j^\alpha}, \tag{S32}$$

where p_j^α can be identified as the modified quasi-momentum in the j-th generalized Brillouin zone of the corresponding bulk.

In practice, it is sufficient to replace e^{ik} with $\beta_{\alpha,j}$ in Eq. (S31), such that

$$\tilde{\nu}^\alpha = \frac{1}{2\pi}\oint dp_j^\alpha \frac{-\tilde{d}_{3,j}^\alpha \frac{\partial \tilde{d}_{2,j}^\alpha}{\partial p_j^\alpha} + \tilde{d}_{2,j}^\alpha \frac{\partial \tilde{d}_{3,j}^\alpha}{\partial p_j^\alpha}}{(\tilde{d}_{3,j}^\alpha)^2 + (\tilde{d}_{2,j}^\alpha)^2}, \tag{S33}$$

where

$$\tilde{d}_{2,j}^\alpha = \cosh\gamma\cos\theta_1^\alpha\sin\theta_2^\alpha + \cos\left(p_j^\alpha - i\ln|\beta_{\alpha,j}(p_j^\alpha)|\right)\cosh\gamma\cos\theta_2^\alpha\sin\theta_1^\alpha + i\sin\left(p_j^\alpha - i\ln|\beta_{\alpha,j}(p_j^\alpha)|\right)\sinh\gamma\sin\theta_1^\alpha \tag{S34}$$

$$\tilde{d}_{3,j}^\alpha = -\sin\left(p_j^\alpha - i\ln|\beta_{\alpha,j}(p_j^\alpha)|\right)\cosh\gamma\cos\theta_2^\alpha + i\cos\left(p_j^\alpha - i\ln|\beta_{\alpha,j}(p_j^\alpha)|\right)\sinh\gamma \tag{S35}$$

The integration in Eq. (S33) is over the j-th generalized Brillouin zone. However, we have numerically checked that $\tilde{\nu}^\alpha$ calculated along different generalized Brillouin zones of a given bulk are the same. We therefore drop the index j on the left-hand side of Eq. (S33).

Following the procedure above, both Bloch and non-Bloch winding numbers in an alternative time frame can be calculated with the Floquet operator

$$U' = M^{\frac{1}{2}}GFM^{\frac{1}{2}}. \tag{S36}$$

Denoting the non-Bloch winding numbers of the two bulks as $\tilde{\nu}'^\alpha$, we calculate non-Bloch topological invariants $\tilde{\nu}_0^\alpha$ and $\tilde{\nu}_\pi^\alpha$ through

$$\tilde{\nu}_{0(\pi)}^\alpha = \frac{\tilde{\nu}^\alpha \pm \tilde{\nu}'^\alpha}{2}. \tag{S37}$$

These non-Bloch topological invariants are the same as those calculated using the periodized Floquet operators with branch cuts, and correctly predict the existence and number of topological edge states through the non-Hermitian bulk-boundary correspondence. In Fig. S2, we show a typical comparison between non-Bloch topological invariants calculated using the two methods. Furthermore, we have experimentally confirmed that adopting periodized Floquet operators associated with U' would give the correct non-Bloch bulk-boundary correspondence in the alternative time frame. This is shown in Fig. S3.

Non-Bloch bulk-boundary correspondence for edge states with $\epsilon = 0$

In the main text, we confirm non-Bloch bulk-boundary correspondence for the following three cases: i) only edge states with $\epsilon = \pi$ exist; ii) both types of edge states with $\epsilon = 0$ and $\epsilon = \pi$ exist; iii) no edge state exists. For completeness, we also perform experiments using parameters under which only edge states with $\epsilon = 0$ exist. This is shown in Fig. S4.

Realizing opposite direction of walking

In Figs. 3a-d of the main text, we measure the time-dependent probability distribution of the walker, which reflects the spatial profile of the bulk states which have a finite overlap with the initial walker state. It follows that the asymmetric probability distribution in Figs. 3a-d depends on both the initial state and the coin parameters of the two bulks. Indeed, as we show in the following figure, upon choosing a different set of parameters, the walker goes to negative positions. As an example, we perform new experiments of unitary quantum walk with parameters $\gamma = 0$, $\theta_1^R = 2\pi/5$, $\theta_1^L = \pi/5$, $\theta_2^R = \pi$, and $\theta_2^L = 0$, for different initial states $|\Phi(0)\rangle = |-1\rangle \otimes |0\rangle$ and $|\Phi(0)\rangle = |-1\rangle \otimes |1\rangle$. We show the walker's distribution up to seven steps in Fig. S5, where the walker goes to negative positions. Similar negative-position-centered, asymmetric probability distribution can be found for non-unitary quantum walks with appropriately chosen coin parameters and initial states.

We emphasize that the key message of Fig. 3 of the main text is the localization of the spatial distribution in the presence of loss, which occurs for generic coin parameters and initial states, and is therefore only possible when bulk states are generically localized.

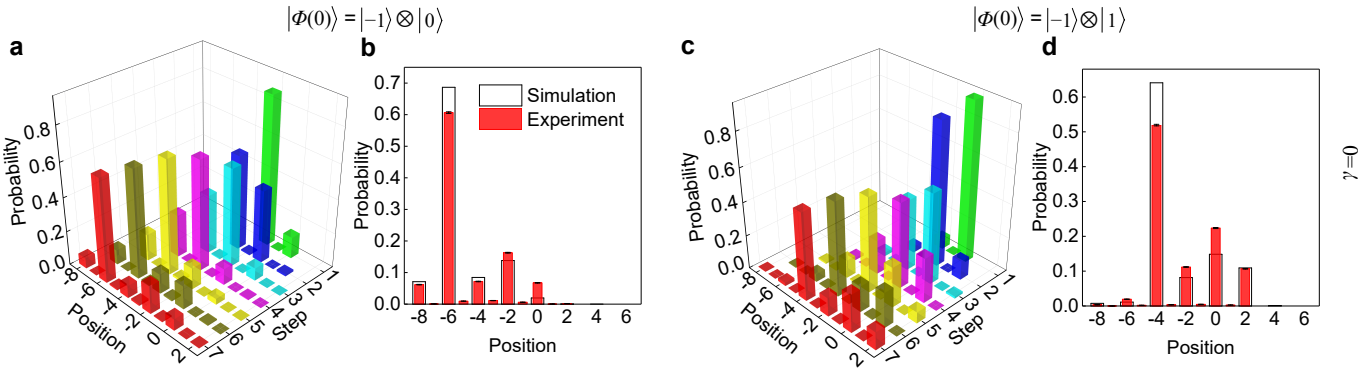

FIG. S5. **Measured probability distribution of unitary quantum walk up to seven steps. a, c** Time-dependent probability distribution of quantum walk with different initial states. **b, d** The distribution at the last step. The coin parameters are $\theta_1^R = 2\pi/5$, $\theta_1^L = \pi/5$, $\theta_2^R = \pi$, and $\theta_2^L = 0$. Error bars represent standard deviations due to photon-counting statistics.

[1] Yao, S. & Wang, Z. Edge states and topological invariants of non-Hermitian systems. *Phys. Rev. Lett.* **121**, 086803 (2018).

[2] Deng, T. & Yi, W. Non-Bloch topological invariants in a non-Hermitian domain-wall system. *Phys. Rev. B* **100**, 035102 (2019).

[3] Asbóth, J. K. & Obuse, H. Bulk-boundary correspondence for chiral symmetric quantum walks. *Phys. Rev. B* **88**, 121406(R) (2013).